



Study on low-frequency fatigue performance of HT700P nickel–iron based high-temperature alloy

Yihang He^{1,2} · Dawei Yi¹ · Jingbo Yan² · Jing Huang¹ · Pei Li¹ · Zheng Yang²

Received: 11 April 2024 / Accepted: 25 June 2024
© Qatar University and Springer Nature Switzerland AG 2024

Abstract

In this study, the low cycle fatigue properties of a new nickel–iron-based superalloy HT700P at different strain amplitudes at 650°C and 700°C were investigated. The results show that at 650°C, with strain amplitudes of 0.3% and 0.7%, the fatigue life of the samples was 17,007 cycles (14 h) and 580 cycles (1.13 h), respectively. At 700°C, the fatigue life was 13,966 cycles (11.65 h) and 469 cycles (0.91 h) for the same strain amplitudes. When the total strain amplitude is 0.3%, the alloy exhibits the behaviour of cyclic softening first, then cyclic hardening and finally cyclic softening. When the total strain amplitude is 0.7%, the alloy exhibits cyclic softening behaviour as a whole. Cyclic softening is related to the continuous cutting of the γ' phase by dislocations and the coarsening of the γ' phase, whereas cyclic hardening is caused by the interaction between dislocations and precipitated phases. By analyzing the fatigue fracture morphology, it can be seen that the fatigue cracks sprouted from the surface of the specimen; when the temperature was 650°C and the total strain amplitude was 0.3% and 0.7%, the fracture morphology of the samples was mainly characterized by the fatigue glow and extended inwardly in the mode of transgranular mode. The microscopic mechanism of low-week fatigue in HT700P high-temperature alloy is plane slip.

Keywords Nickel-based superalloy · Low-cycle fatigue · Cyclic hardening · Cycle softening · Fracture topography

1 Introduction

The annual development report of China's power industry 2021 shows that the installed capacity of coal power accounts for 49% of the total installed capacity, and its power generation accounts for 61% of the total power generation. In the future, China's coal-fired thermal power generation will continue to occupy the main share of total power generation [1]. It is found that improving the steam parameters during the operation of thermal power units can effectively improve the power generation efficiency of thermal power units [2, 3]. The steam parameters affecting the thermal efficiency of thermal power units are mainly temperature and pressure. The higher the two parameters are, the higher the

efficiency of the unit is. Therefore, higher requirements are put forward for the candidate materials of high-temperature units. Nickel-based superalloys and nickel–iron-based superalloys are usually considered candidate materials for high-temperature components of thermal power units due to their excellent high-temperature properties [4, 5].

Currently, both domestic and international organizations have conducted extensive research on high-temperature candidate materials. The European AD700 project conducted performance studies on alloys such as IN617, IN740, and Haynes263, and finally chose IN617 as the material for the 700°C high-temperature jacket, subsequently improving it to obtain materials such as IN617B and IN617BOCC [2, 6, 7]. The United States optimized the composition of the IN740 alloy to control the G-phase precipitation, resulting in the improved IN740H alloy [8]. The improved alloy ensures the precipitation of the γ' phase while slowing the growth rate of the reinforcing phase, providing better high-temperature stability than its predecessors [6]. In Japan, the "New Sunshine" program selected HR6W as the main steam pipe and turbine rotor material for A-USC power stations [9].

Due to the non-uniformity of electricity loads, the function of many thermal power units is shifting from primary power

✉ Dawei Yi
yidawei19820608@163.com

✉ Jingbo Yan
yf625oscar@163.com

¹ School of Materials Science and Engineering, Xi'an University of Science and Technology, Xi'an 710032, China

² Xi'an Thermal Engineering Research Institute Co., LTD., Xi'an 710054, China

generation to peak load regulation. Frequent starting and stopping of the units, along with peaking mode realized through variable voltage, leads to excessive transient load changes and drastic temperature fluctuations, making the main steam piping susceptible to low-cycle fatigue. Therefore, anti-fatigue design is crucial for improving the high-temperature service performance of thermal power units.

Foreign research on the low-cycle fatigue of nickel-based high-temperature alloys began earlier. Huang et al. [10] conducted monotonic tensile strain and cyclic loading deformation tests on C-22HSTM alloy and found that dislocation hardening is the main reinforcement mechanism in these experiments. Pang et al. [11] investigated the effect of Udimet 720 alloy microstructure on room temperature fatigue crack initiation and short crack extension, concluding that fatigue cracks occurred due to slip band cracking and surface or sub-surface voids. Enhancing fatigue crack initiation and resistance to crack extension could increase the alloy's fatigue life. Li et al. [12] found that for 316LN alloy, within the range of 350°C to 550°C, increasing the temperature raised the cyclic stress amplitude and decreased the strain rate, promoting dynamic strain aging. This ultimately facilitated planar slip of dislocation motion, inhibited cross-slip, and increased the plastic deformation resistance of the material. Xiao et al. [13] studied the cyclic deformation mechanism of IN718 and pointed out that the deformation caused by the plane slip band is attributed to the paired dislocation shear of continuous and ordered precipitated γ'' and γ' phases. After the initial shear, the size of the precipitated phase decreases, resulting in the reduction of deformation resistance, resulting in the formation of a plane slip zone. Clavel et al. [14] showed that the precipitated phase in IN718 was shear and plastic during cyclic deformation. The deformation is caused by the expansion of planar slip bands, which are identified as twins. Fournier [15] studied the low-cycle fatigue performance of IN718 at room temperature and 550°C, and found that the fatigue life decreased when the temperature increased from room temperature to 550°C, and the fatigue life further decreased when the frequency decreased from 3 cycle/min to 0.3 cycle/min under high temperature conditions. At low temperature, the material first appears a short hardening phenomenon, and then becomes a continuous softening; At high temperature, the material only softens.

In China, research on the low-cycle fatigue of nickel-based high-temperature alloys began relatively late. Chen et al. [16] studied the room temperature fatigue properties of GH4169 high-temperature alloys and discovered that the cyclic hardening rate initially increased and then decreased with increasing strain amplitude, while the cyclic softening rate showed the

opposite trend. Xie et al. [17] found that K416B alloy exhibits a transition fatigue life at room temperature and 900°C, with cyclic life exceeding the transition fatigue life. Zhou et al. [1] compared the high-temperature low-cycle fatigue performance of Inconel617 and C-HRA-2 alloys, showing that the material's cyclic stress response and fatigue life are related to strain amplitude. Alice et al. [18] studied the microscopic damage and fracture mechanisms of nickel-based single-crystal high-temperature alloys under low-cycle fatigue, finding that low strain conditions at high temperatures could reduce the fatigue performance of single-crystal alloys.

However, most of the current studies are conducted on the fatigue analysis of existing nickel-based alloys, and the understanding of the fatigue behavior and mechanism of nickel-iron base superalloys under high temperature environment is not deep enough. With the emergence of new superalloy materials, the fatigue characteristics and influencing factors of these materials also need to be further explored. Due to the high cost of nickel-based superalloy, China has comprehensively considered the performance and cost of materials, and proposed nickel-iron based superalloy as a candidate material for high-temperature components of thermal power units. The fatigue deformation mechanism and failure mode of HT700P alloy under different strain amplitudes at 650°C and 700°C are discussed in this study. The purpose of this study is to elucidate the fatigue mechanism and influencing factors of nickel-iron based superalloys, and to provide support for their application and development.

2 Test materials and methods

2.1 Test material

The experimental material is a nickel-iron-based HT700P high-temperature alloy, which was developed by Xi'an Institute of Thermal Engineering Research Co., Ltd. The ingots were cast using vacuum induction followed by vacuum self-consumption duplex smelting equipment, and then hot extruded and molded through forging of open billets. The chemical compositions of the alloys are shown in Table 1. After the alloy was hot-extruded and molded, it underwent solution treatment. The solution treatment regimes involved holding at 1000°C-1100°C for 100 min followed by water cooling, and holding at 950°C-1050°C for 60 min followed by water cooling.

The HT700P alloy exhibits a γ' -Fe phase austenitic structure as its matrix, characterized by a face-centered

Table 1 Chemical composition of HT700R alloy

Fe	Cr	Mo+Nb+W	Ti+Al	C	B	Si	Ni
25–45	15–25	≤4.5	1.0–5.0	≤0.1	≤0.01	≤0.5	Bal

cubic (FCC) crystal structure. The main constituents of this alloy are Ni and Fe elements, as depicted in Fig. 1(a). The strengthening phase of the alloy is primarily attributed to the long-range ordered face-centered cubic structure known as the γ' phase, illustrated in Fig. 1(b). In this phase, Ni occupies the face-centered position, while Al resides at the vertex position. The HT700P alloy phase primarily consists of a matrix γ [fcc-Fe(Ni)], while the strengthening phase is represented by γ' [Ni₃Al or Ni₃(Al, Ti), etc.].

2.2 Test Methods

The prepared ingots were initially wire-cut to produce M14 fatigue samples, following the standard GB/T 5782–2016, as depicted in Fig. 2. The fatigue experimental test was conducted in accordance with the standard reference GB/T 15248–2008 "Method for axial equal amplitude low cycle fatigue testing of metal materials" using the Landmark-40 fatigue testing machine. The strain control employed an axial tensile compression ratio of -1, with a triangular waveform selected for loading. Strain amplitudes of 0.15%, 0.3%, 0.5%, 0.7%, and 0.9% were tested at temperatures of 650 °C and 700 °C, respectively. Fatigue failure was determined by specimen fracture.

The microstructure of the fatigue deformation region was examined using a JEM-2100 transmission electron microscope (TEM). For TEM sample preparation, thin slices were obtained from approximately 1 mm away along the loading axis direction from the fracture surface using a SYJ-400 type low-speed diamond grinder. These thin slices had an initial

thickness of around 0.5 mm and were subsequently ground to approximately 50 μ m. They were then further thinned using the MTP-1A magnetically driven double-jet electrolytic thinning device, with a 9% perchloric acid solution selected as the electrolytic medium. The applied voltage for double-jet was set at 22 V while maintaining a controlled temperature of -25°C. Finally, a Zeiss Sigma-HD scanning electron microscope (SEM) was employed to observe both the fatigue fracture morphology and microstructure.

3 Results

3.1 Fatigue life curve

The fatigue curves of HT700P alloy under different strain amplitudes (0.15%, 0.3%, 0.5%, 0.7%, 0.9%) at temperatures of 650°C and 700°C are depicted in Fig. 3. The horizontal axis represents the number of failure reversals ($2N_f$), while the vertical axis denotes the magnitude of the strain amplitude. Within the figure, three distinct curves can be observed: the black line represents the overall strain-life curve, the blue line indicates the plastic strain-life curve, and the red line depicts the elastic strain-life curve.

Fatigue life relationship formula:

The Basquin's formula:

$$\frac{\Delta\sigma}{2} = \sigma_f'(2N_f)^b \quad (3-1)$$

Equation for the elastic component relationship between stress and strain:

Fig. 1 Crystal structure (a) Crystal structure of γ phase (b) Crystal structure of γ' phase

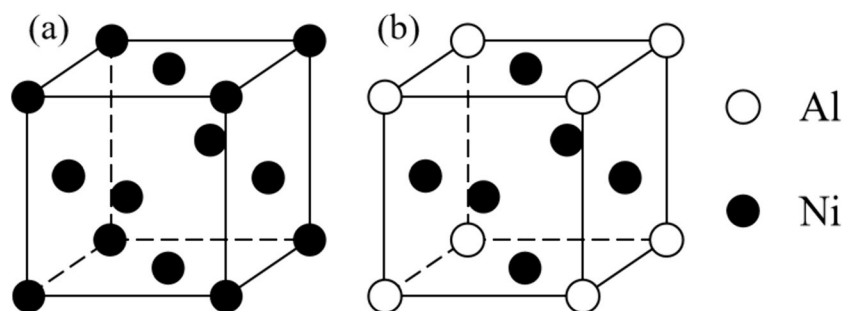


Fig. 2 M14 Fatigue Sample Size

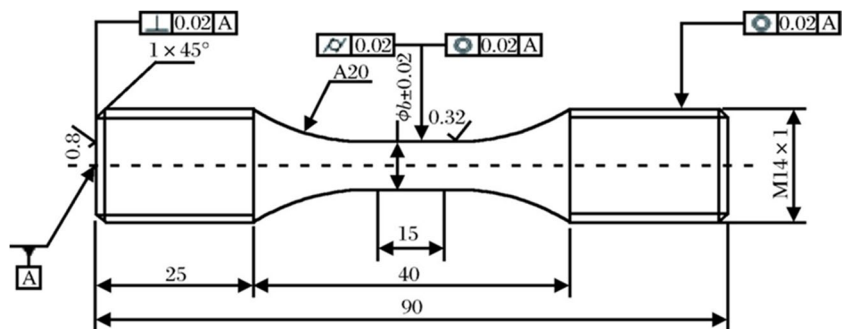
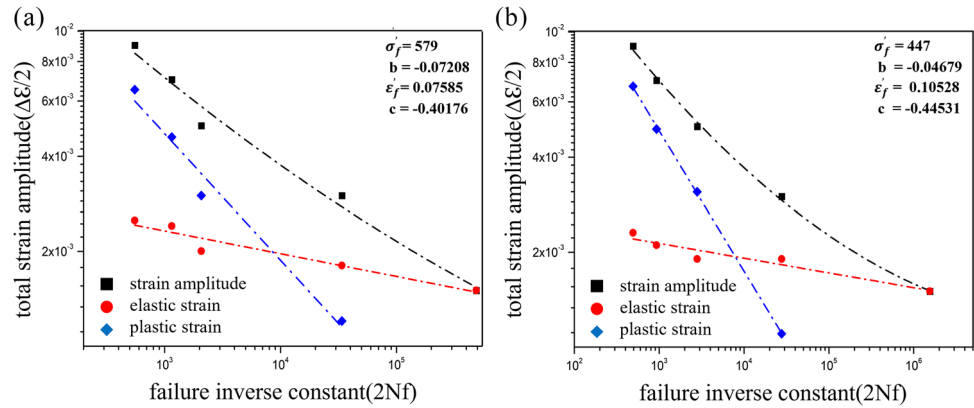


Fig. 3 Strain-fatigue life curves of HT700P alloy at 650 °C and 700 °C (a) 650 °C (b) 700 °C



$$\Delta \varepsilon_e = \frac{\Delta \sigma}{E} \quad (3-2)$$

Combining Eqs. (3-1) and (3-2):

$$\frac{\Delta \varepsilon_e}{2} = \frac{\sigma_f'}{E} (2Nf)^b \quad (3-3)$$

The Manson-coffin formula:

$$\frac{\Delta \varepsilon_p}{2} = \varepsilon_f' (2Nf)^c \quad (3-4)$$

The total strain is the sum of the elastic and plastic strains:

$$\frac{\Delta \varepsilon}{2} = \frac{\Delta \varepsilon_e}{2} + \frac{\Delta \varepsilon_p}{2} \quad (3-5)$$

Deriving the strain-life relationship formula:

$$\frac{\Delta \varepsilon}{2} = \frac{\sigma_f'}{E} (2Nf)^b + \varepsilon_f' (2Nf)^c \quad (3-6)$$

E is the elastic modulus, b is the fatigue strength index (Basquin index), which is the slope of the elastic strain line in Fig. 3. σ_f' is the fatigue strength coefficient, which is the product of the intercept of the elastic strain line and the elastic modulus. c is the fatigue ductility index (Manson-coffin index), which is the slope of the plastic strain line. ε_f' is the fatigue ductility coefficient (plastic strain amplitude when $2Nf=1$) and is the intercept of the plastic strain line in Fig. 3.

Using formula (3-6), the values determined for Fig. 3(a) are $\sigma_f' = 579$, $b = -0.07208$, $\varepsilon_f' = 0.07585$,

and $c = -0.40176$. Similarly, for Fig. 3(b), the values are $\sigma_f' = 447$, $b = -0.04679$, $\varepsilon_f' = 0.10528$, and $c = -0.44531$. The figure demonstrates that at low strain amplitudes, the alloy predominantly undergoes elastic deformation during fatigue, whereas at high strain amplitudes, plastic deformation becomes more significant. Comparing the results, it is evident that strain amplitude has a more pronounced effect on fatigue life than temperature.

The experimental results of low cycle fatigue of HT700P alloy under different strain amplitudes at 650 °C and 700 °C are presented in Table 2. It can be observed from the table that when the strain amplitude is 0.3%, the sample exhibits a higher life with failure cycles of 17,007 times (650 °C) and 13,966 times (700 °C), along with an experimental time of 14 h (650 °C) and 11.65 h (700 °C). Conversely, when the strain amplitude increased to 0.7%, the fatigue life sharply decreased, resulting in failure cycles of only 580 times (650 °C) and 469 times (700 °C), accompanied by an experimental time of merely 1.13 h (650 °C) and 0.91 h (700 °C). These results indicate that while temperature has a relatively minor effect on the fatigue life of the samples, while strain amplitude serves as the primary factor affecting fatigue life.

3.2 Cyclic Stress Curves at Different Temperatures and Strain Amplitudes

Figure 4 presents the cyclic stress response curves of HT700P alloy at 650 °C with different strain amplitudes. As depicted in Fig. 4(a), at a temperature of 650 °C and a strain range of 0.3%, the initial fatigue stage exhibits a rapid

Table 2 Low cycle fatigue test results of HT700P alloy at 650 °C and 700 °C

Strain amplitude and temperature	Strain ratio	Experimental frequency (Hz)	Cycle of failure(Nf)	Time(h)	Result
650 °C-0.3%	-1	0.333	17,007	14	fracture
650 °C-0.7%	-1	0.143	580	1.13	fracture
700 °C-0.3%	-1	0.333	13,966	11.65	fracture
700 °C-0.7%	-1	0.143	469	0.91	fracture

decline in stress, indicating cyclic softening behavior of the alloy during this period. Subsequently, as the stress drops to approximately 670 MPa, it steadily increases, suggesting cyclic hardening behavior of the alloy matrix at that point. Notably, after reaching around 10,000 cycles, a short-lived cyclic hardening phenomenon can be observed in the cyclic stress response curve of the tested alloy. In the later stages of fatigue deformation, there is a gradual decrease in cyclic stress within the alloy matrix with increasing cycles until it rapidly decreases due to crack initiation and propagation, leading to sample failure. As shown in Fig. 4(b), when subjected to a temperature of 650°C and a strain range of 0.7%, the alloy demonstrates continuous cyclic softening throughout its fatigue deformation process. However, after approximately 300 cycles, there is a brief episode of cyclic hardening before gradually decreasing again until final fracture.

As shown in Fig. 5, the cyclic stress response curves of HT700P alloy at 700°C with different strain amplitudes. As depicted in Fig. 5(a), at a temperature of 700°C and a strain amplitude of 0.3%, the sample's stress exhibits an initial rapid decline during the fatigue stage. Subsequently, when the stress reaches approximately 700 MPa, it shows a steady increasing trend, indicating cyclic hardening behavior within the alloy matrix. Upon reaching a cycle count of 13,000 cycles, the cyclic stress gradually decreases until crack initiation and propagation cause a rapid drop leading to sample failure. Similarly observed in Fig. 5(b) is that at a temperature of 700°C and with a strain amplitude of

0.7%, the sample's stress initially decreases from an initial value of 900 MPa to around 800 MPa during the first twenty-week cycle stage before entering into a saturation phase. After cycling for approximately 125 cycles, it enters into a softening stage.

The stress–strain curves of HT700P alloy at different strain amplitudes at 650°C and 700°C are illustrated in Fig. 6. It is illustrated that a single cyclic stress results in a monotonic relationship between stress and strain. Under tensile strain, the stress increases with increasing strain, while under compressive strain, the stress decreases upon unloading of the strain. The cyclic curve of the alloy exhibits distinct hysteresis characteristics, forming a closed fusiform shape in the cyclic stress–strain diagram [19]. This indicates the excellent plastic deformation ability of the alloy material. The enclosed area [20] within this hysteresis loop during fatigue cycle deformation represents energy loss after one cycle, which increases with higher strain amplitude, indicating that each fatigue cycle with greater strain amplitude requires more energy expenditure. Furthermore, asymmetry is observed in the tensioning process of the stress–strain curves at 650°C and 700°C due to the viscoelastic behavior exhibited by the alloy material: elastic deformation occurs within its elastic limit when subjected to strains under applied stresses; however, due to energy dissipation during deformation processes, there is an asymmetry between the rising and falling sections of the strain curve [21].

Fig. 4 Cyclic stress curves of HT700P alloy at 650 °C with different strain amplitudes: (a) 0.3%, (b) 0.7%

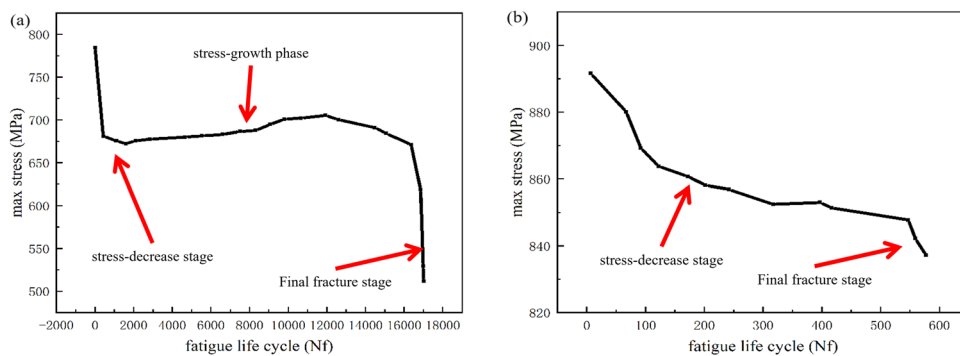


Fig. 5 Cyclic stress curves of HT700P alloy at 700 °C with different strain amplitudes: (a) 0.3%, (b) 0.7%

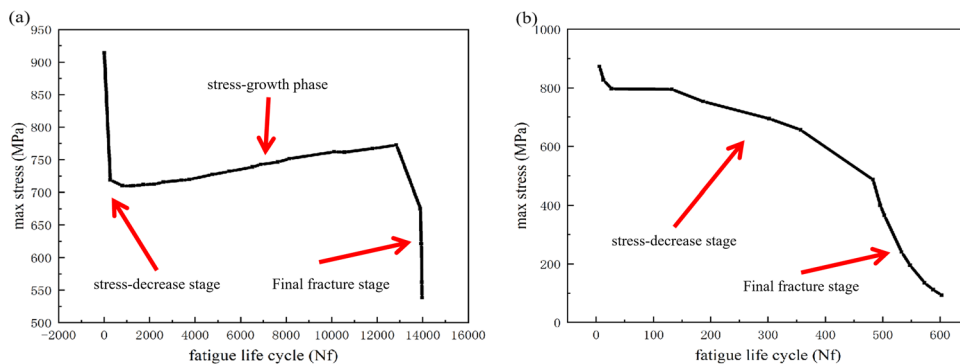
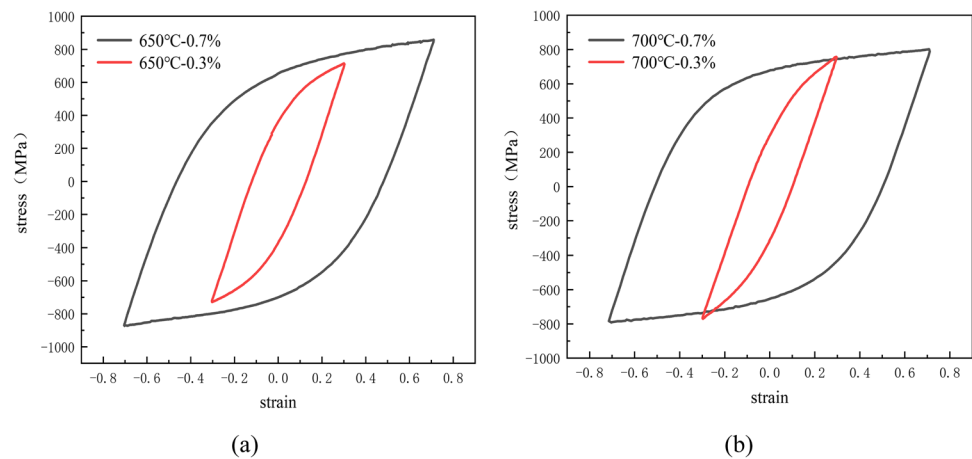


Fig. 6 Hysteretic curves of HT700P alloy with different strain amplitudes at 700°C: (a) 0.3%, (b) 0.7%



3.3 Precipitation of the intragranular strengthening γ' phase at different temperatures with different strain amplitudes

Table 3 presents the experimental results of γ' phase size in HT700P alloy after aging treatment at 650°C and 700°C, respectively. It can be observed from the table that when the aging temperature is set at 650°C, an increase in aging time from 12 to 100 h leads to a corresponding growth in γ' phase size from 7.49 nm to 18.09 nm. Similarly, for an aging temperature of 700°C, the γ' phase size increases from 10.67 nm to 26.013 nm as the aging time extends from 12 to 100 h.

According to the Lifshitz-Slyozov-Wagner theory, the phenomenon can be interpreted as [22, 23]:

$$r^3 - r_0^3 = kt \quad (4-1)$$

The rate constant, denoted as k , can be mathematically expressed as follows:

$$k = \frac{8aC V_f^2 D_s}{9R_g T} \quad (4-2)$$

Table 3 Experimental results of γ' phase size of HT700P alloy after aging treatment at 650°C and 700°C

Temperature (°C)	Aging time (h)	The dimension of γ' (nm)
650	100	18.09
650	50	13.22
650	24	10.37
650	12	7.49
700	100	26.013
700	50	20.059
700	24	14.73
700	12	10.09

where r is the average radius of the precipitated phase at different ageing times, r_0 is the radius of the initial precipitated phase, a is the surface energy, C is the solubility of the solute, V_f is the volume fraction of the particles, D_s is the elemental diffusion coefficient, t is the ageing time, R_g is the ideal gas constant, and T is the absolute temperature.

According to the formula, Fig. 7 illustrates the r^3 - t relationship curve of γ' phase at temperatures of 650°C and 700°C. By means of linear fitting, it can be observed that the cubic power of γ' phase radius exhibits a linear correlation with aging time, indicating that the precipitation and growth behavior of γ' phase in HT700P alloy adheres to LSW diffusion theory. By extrapolating the two fitting curves in Fig. 7, it can be observed that at a temperature of 650°C, γ' phase precipitation initiates after an aging duration of 7.8 h. Similarly, at a temperature of 700°C, γ' phase precipitation initiates after an aging duration of 6.2 h.

Figure 7 shows the transmission picture of the sample at 700°C, 0.3% strain amplitude, and illustrated the transmission spot picture of the γ' phase. It can be seen from the picture that there are many round small particles around the dislocation at this time. In order to determine the surrounding fine particles, the transmitted light spot image of the particles is added. By calculations, it is found that the lattice constants of the particle structure in the inset figure of Fig. 8 are $a_{100} \approx 0.358$ nm, $a_{\bar{2}00} \approx 0.358$ nm, $a_{\bar{1}\bar{1}\bar{1}} \approx 0.359$ nm, and $a_{\bar{1}\bar{1}\bar{1}} \approx 0.359$ nm which match the lattice constant $a = 0.357$ nm of γ' (Ni₃Al) in the PDF card. Therefore, it can be determined that the particles in the TEM image are the γ' phase.

Figure 9 shows the morphology of the intragranular strengthening γ' phase of HT700P alloy at 650°C with different strain amplitudes. From Fig. 9(a), it can be observed that the average size of the intragranular strengthening γ' phase is 7.32 nm when the temperature is 650°C and the strain amplitude is 0.3%. Although the density of γ' phase is higher, its size is smaller. In contrast, the reinforced γ' phase

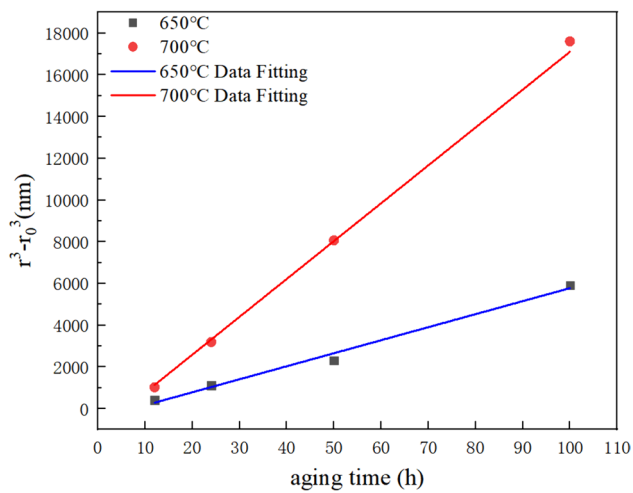


Fig. 7 r^3-t relationship curves of γ' phase at different aging temperatures.

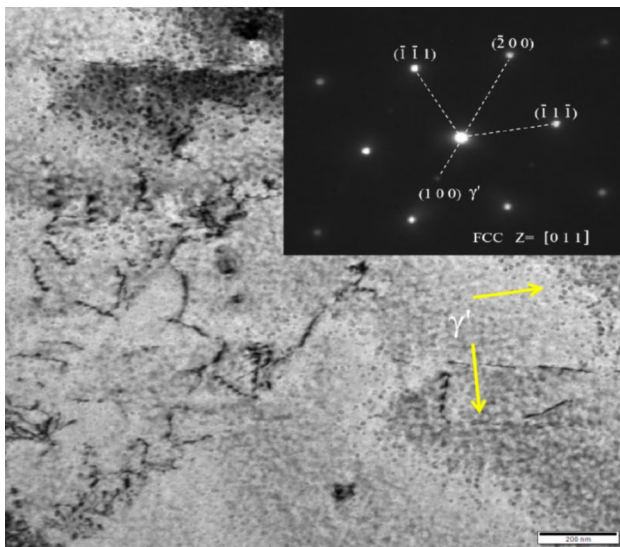
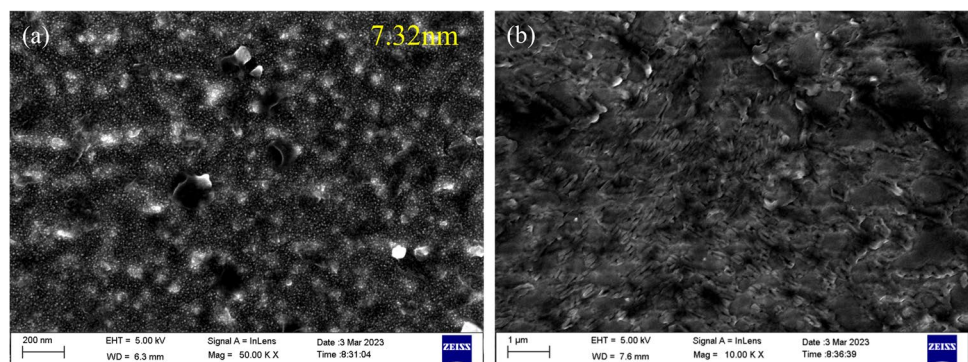


Fig. 8 TEM image displaying the γ' phase particles, the insertion picture is the diffraction spot of the γ' phase

Fig. 9 Morphology of the intragranular strengthening γ' phase in HT700P alloy at 650 °C with different strain amplitudes: (a) 0.3%, (b) 0.7%



is not observed in Fig. 9(b), indicating that the size of the reinforced γ' phase is too small or it has not precipitated yet.

Figure 10 shows the morphology of the intragranular strengthening γ' phase in HT700P alloy under different strain amplitudes at 700°C. In Fig. 10(a), the size of the intragranular strengthening γ' phase is 16.67 nm, which is significantly larger than that of γ' phase at 650°C. The particles are spherical, with a higher density and smaller spacing between particles. Figure 10(b) also does not show the reinforced γ' phase, indicating that the size of the reinforced γ' phase is too small or it has not precipitated yet.

3.4 Microstructure of HT700P alloy profile

Figure 11 shows the sectional microstructure of HT700P alloy when the strain amplitude is 0.3%. As seen in Fig. 11(a), at a temperature of 650°C, a large number of parallel slip bands with high density appear in the grain, and the intersection of slip bands in two directions occurs locally. When the slip bands move to the grain boundary, they cannot cross it. In Fig. 11(b), it can be observed that at 700°C, numerous parallel slip bands with higher density appear in the crystal, but there is no interaction between the slip bands. When the slip bands move to the twin grain boundary, they cannot cross the twin grain boundary. When the strain amplitude is 0.7%, no slip bands are found in the sample, indicating that the crack propagation rate is faster, making intercrystalline deformation less obvious.

Figure 12 shows the dislocation grouping of the samples at 650 °C for different strain amplitudes. Figure 12(a) and (b) illustrate the dislocation patterns of the sample at 650 °C with a strain amplitude of 0.3%. From Fig. 12(a), it can be seen that dislocations exist inside the alloy matrix grains, and dislocations cannot cross the grain boundaries, indicating that the grain boundaries hinder dislocation motion. Additionally, a large number of dislocation walls can be observed in Fig. 12(b), showing typical plane slip characteristics. It can be assumed that the fatigue deformation mechanism of HT700P Ni–Fe-based high-temperature

Fig. 10 Morphology of the intragranular strengthening γ' phase in HT700P alloy at 700 °C with different strain amplitudes: (a) 0.3%, (b) 0.7%

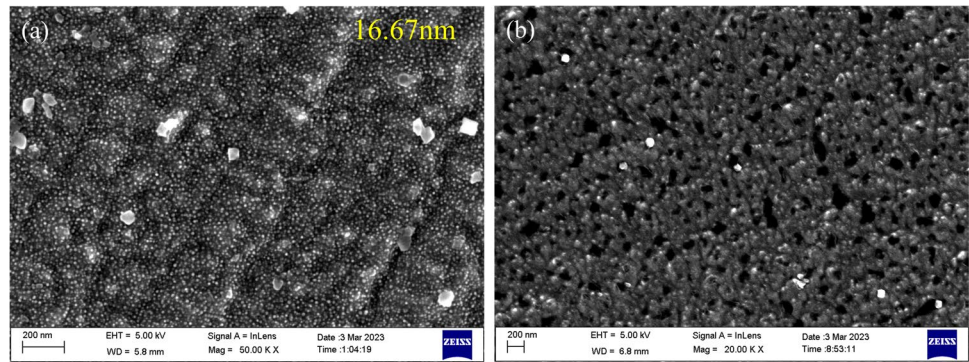
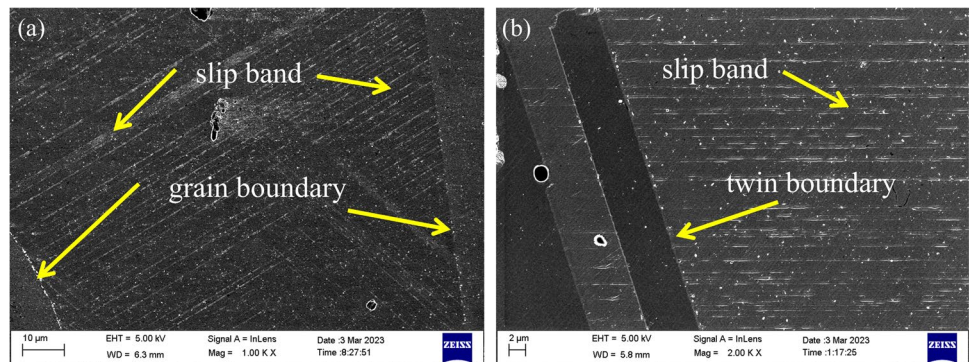


Fig. 11 Microstructures of HT700P alloy 0.3% strain amplitude profiles at different temperatures: (a) 650 °C, (b) 700 °C



alloy matrix at 650 °C when the strain amplitude is 0.3% is plane slip.

The dislocation grouping of the sample at 650 °C with a strain amplitude of 0.7% is shown in Fig. 12(c) and (d). From Fig. 12(c), it can be observed that localized dislocation plugging can hinder dislocation movement, but most of the dislocations are more uniformly distributed. The dislocation density is relatively lower than that in Fig. 12(a), with most being flat dislocations and without any obvious entanglement between them.

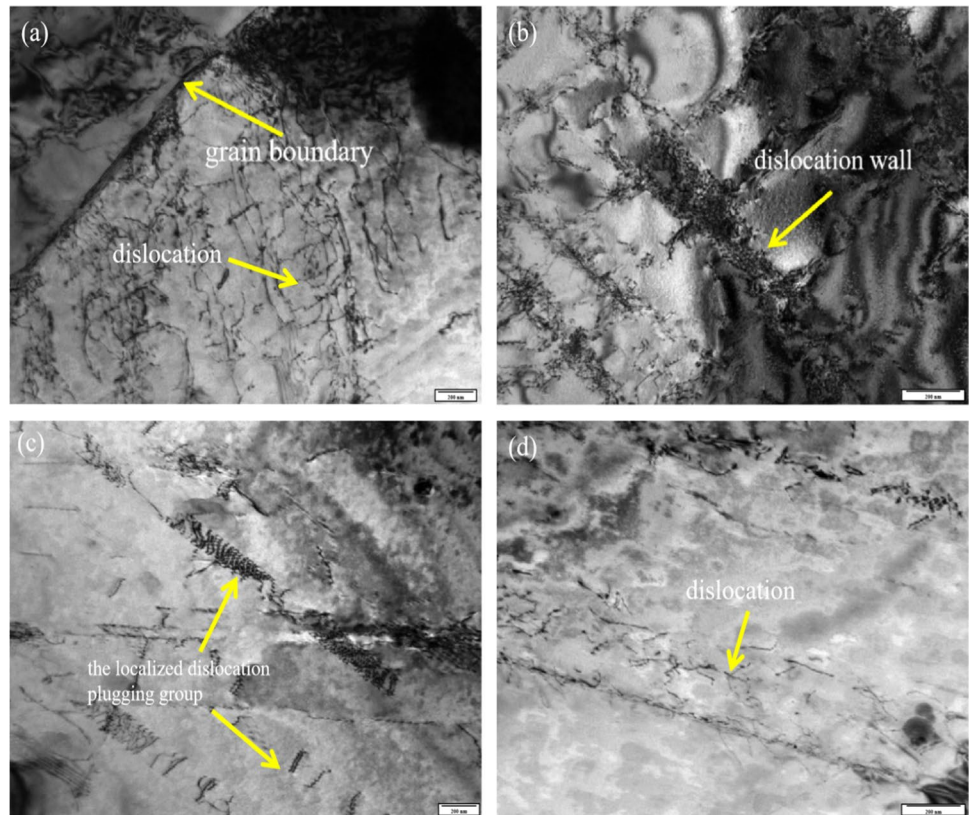
Figure 13 shows the dislocation grouping of the samples at 700 °C for different strain amplitudes. The dislocation groupings of the sample at 700 °C with a strain amplitude of 0.3% are shown in Fig. 13(a), (b), and (c). As seen in Fig. 13(a), some dislocations cut through the γ' phase particles from the center, while others move to the side of the γ' phase particles without cutting through them, leaving the γ' phase particles intact. A large number of Persistent Slip Bands (PSBs) are observed in the crystal, showing typical plane slip characteristics. It can be concluded that the fatigue deformation mechanism of the HT700P Ni–Fe-based high-temperature alloy matrix at 700 °C with a strain amplitude of 0.3% is plane slip. From Fig. 13(c), it can be observed that there is a high-density dislocation region inside the alloy

with a dense dislocation distribution and localized dislocation entanglement. Figure 12(d) and (e) show the dislocation grouping state of the sample at 700 °C with a strain amplitude of 0.7%. As seen in the figures, most dislocations exist in the form of single monoclinic dislocation lines, with dislocation entanglement found only in localized areas, and dislocation walls are not observed.

3.5 Fracture morphology under different strain amplitudes

Figure 14 shows the fracture morphology, crack source area, and expansion area of HT700P alloy under different strain amplitudes at 650 °C. Figure 14(a) and (b) illustrate the fracture morphology of the samples with strain amplitudes of 0.3% and 0.7%, respectively. It can be observed that the fatigue fracture of the specimen exists in three typical zones: the fatigue source area, the crack expansion area, and the final instantaneous fracture area. The fatigue source area occurs on the surface of the specimen and is the flattest area of the fracture. Figure 14(c) and (d) show the fatigue source areas of the samples with strain amplitudes of 0.3% and 0.7%, respectively. It can be observed that the fatigue cracks originate on the surface

Fig. 12 Dislocation grouping of HT700P alloy at 650 °C with different strain amplitudes: (a), (b) 0.3%; (c), (d) 0.7%



of the samples, and the fatigue source area shows an obvious radial texture. Figure 14(e) and (f) depict the crack extension areas of the samples with strain amplitudes of 0.3% and 0.7%, respectively. A large number of fatigue striations can be observed, and it is found that the perpendicular direction of the fatigue striations is parallel to the radiation point of the fatigue source area. This indicates that the vertical direction of the fatigue striations corresponds to the direction of fatigue crack extension. Comparing the samples with strain amplitudes of 0.3% and 0.7%, it is found that the area of the crack extension zone decreases with the increase in strain amplitude, and the spacing between fatigue striations increases.

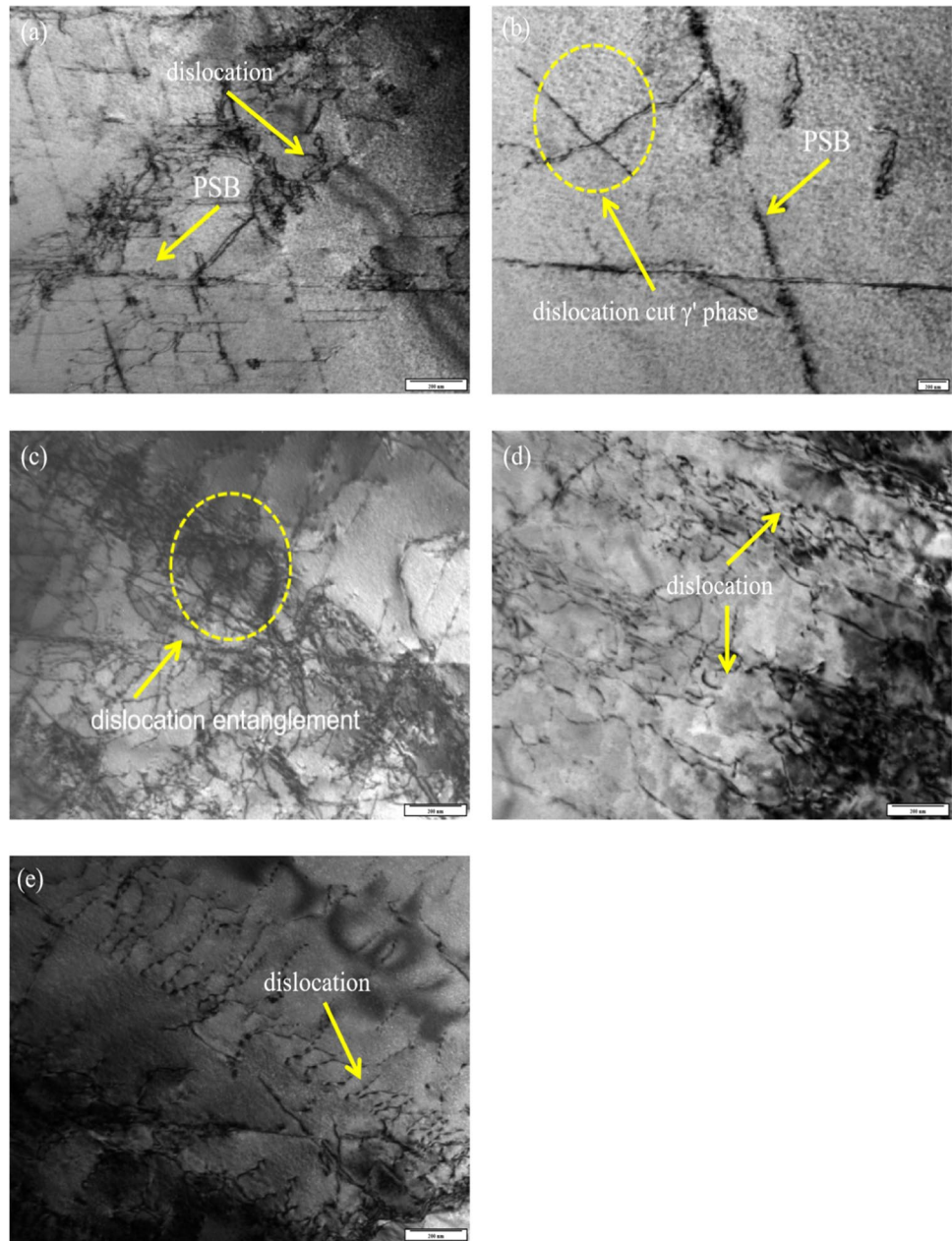
Figure 15 shows the fracture morphology, crack source area, and expansion area of HT700P alloy under different strain amplitudes at 700 °C. Figure 15(a) and (b) illustrate the fracture morphology of the samples with strain amplitudes of 0.3% and 0.7%, respectively. It can be seen that the fatigue fracture of the specimen exists in three typical zones: the fatigue source area, the crack expansion area, and the final instantaneous fracture area. Figure 15(c) and (d) show the fatigue source areas of the samples with strain amplitudes of 0.3% and 0.7%, respectively. From Fig. 15(c), it can be observed that the fatigue cracks sprouted on the surface of the sample, with the radial texture of the fatigue source

zone being not obvious. In Fig. 15(d), it can be observed that the fatigue cracks sprouted on the surface of the sample, but there are also characteristics of intergranular fracture. Figure 15(e) and (f) depict the crack extension areas of the samples with strain amplitudes of 0.3% and 0.7%, respectively. From Fig. 15(e), it can be seen that when the strain amplitude is 0.3%, only localized fatigue striations appear. From Fig. 15(f), when the strain amplitude is 0.7%, secondary cracks appear, and fatigue striations appear only in localized areas.

4 Discussions

Due to stress concentration and repeated loading, slip systems (primarily the slip plane and direction in face-centered cubic crystals) begin to move within the grain, forming a slip zone. The accumulation and interaction of dislocations within this zone under cyclic stress lead to local strain concentration. When encountering obstacles such as grain boundaries or second-phase particles, these high-strain zones intensify, initiating micro-cracks [24, 25], as shown in Fig. 16.

Fig. 13 Dislocation grouping of HT700P alloy at 700 °C with different strain amplitudes: (a), (b), (c) 0.3%; (d), (e) 0.7%

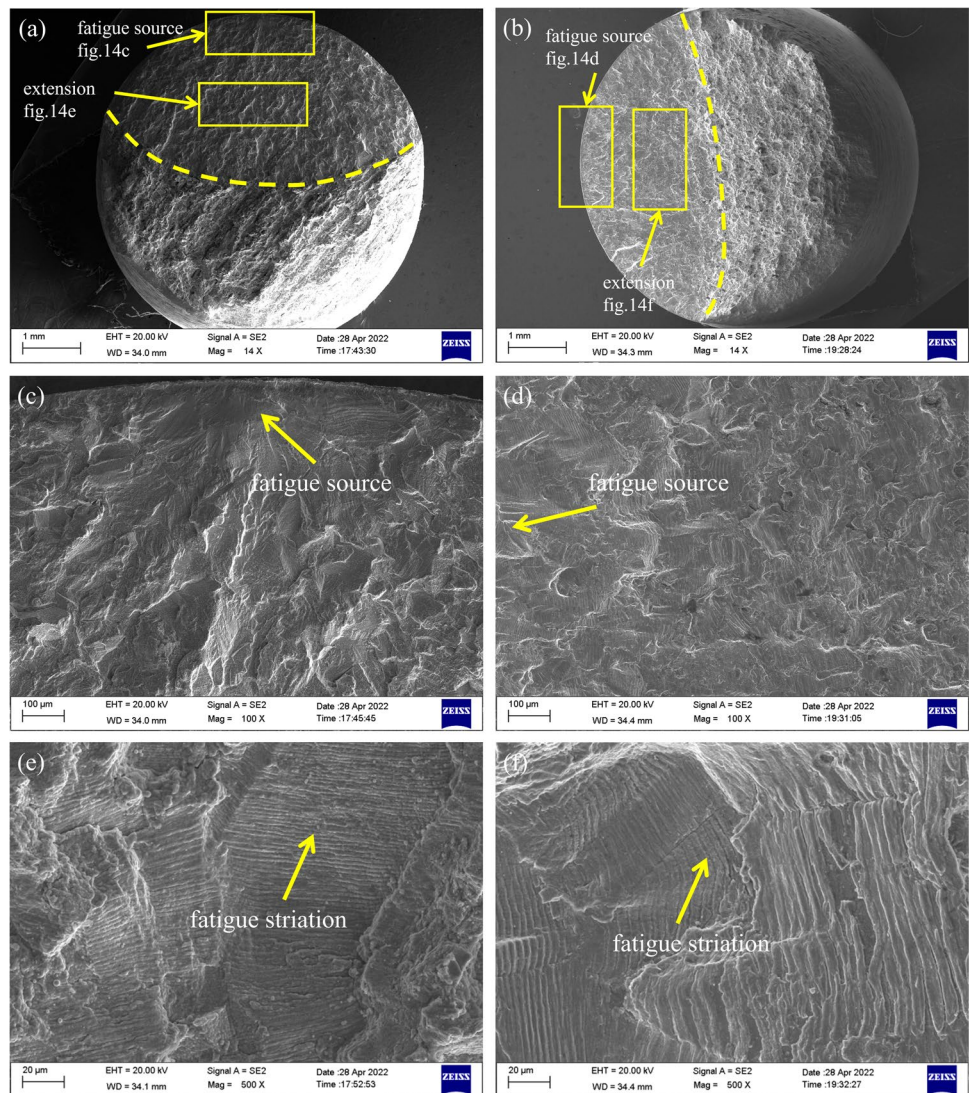


Once a microcrack is initiated, it will propagate along the slip zone in a continuous manner. This propagation process can be divided into two stages: Stage 1: The microcrack expands either within the slip zone or in the direction of the principal stress axis through shear deformation. During this stage, the growth rate of the crack is relatively slow and primarily influenced by dislocation activity within the slip zone [26, 27]. Stage 2: As the microcrack extends to a certain extent, it merges with other cracks to form larger cracks. At this point, the crack growth mode transitions to the opening mode, resulting in a significant acceleration of the crack propagation rate [28]. Moreover, the path of crack extension tends to align perpendicular to the principal stress direction.

The effective section of the sample gradually decreases as the fatigue crack continues to propagate, leading to final fracture when the remaining section is unable to withstand the increasing stress [25], as shown in Fig. 17.

KIM et al. [29] compared the fatigue crack extension rates of different sizes of γ' phase in RR1000 alloy at 650 °C and found that the fatigue crack extension rates of alloys with larger sizes of γ' phase were higher than those of alloys with smaller sizes of γ' phase under the same stress level. WANG et al. [30] found that, when aging at 700 °C and 750 °C, the fatigue crack extension rates of the GH4586 alloy increase and the crack extension path gradually becomes straight. By comparing the fracture morphology of the 0.3% strain

Fig. 14 Fracture morphology of HT700P alloy at different strain amplitude at 650 °C: (a), (c), (e) 0.3%; (b), (d), (f) 0.7%



amplitude samples, it can be found that the fracture morphology of the sample at 650 °C (Fig. 14a) is relatively smooth and the crack source is radial, while the fracture morphology of the sample at 700 °C (Fig. 15a) is relatively rough and the radial texture of the crack source is not obvious. In this case, the γ' phase size of the sample at 700 °C (16.67 nm) is larger than that at 650 °C (7.32 nm); and the fatigue life of the sample at 700 °C (11.65 h) is lower than that at 650 °C (14 h). This indicates that under the same strain amplitude, the larger the γ' phase size, the faster the crack extension rate, the shorter the fatigue life of the material, and the larger the roughness of the fatigue fracture surface.

HT700P NiFe-based high-temperature alloy mainly exhibits two phases of cyclic hardening and cyclic softening during low-cycle fatigue at high temperatures with different strain amplitudes. It was found [11, 31, 32] that the fine γ' phase precipitated phase was repeatedly cut by dislocations

during cyclic deformation, which reduced the effective size of the γ' phase on the slip surface, thus reducing the external force required for the dislocations to cut through the γ' phase, ultimately forming a dislocation-prone slip channel with very little resistance, which induced cyclic softening. At the same time, both the fine γ' phase and the high volume fraction γ' phase enhance the slip reversibility of the alloy, thereby reducing the degree of fatigue damage accumulation and improving the crack extension resistance of the alloy. The sharp softening of the samples with a strain amplitude of 0.3% at the early stage of fatigue may be related to the smaller size of the reinforcing phase γ' phase in their structures because the smaller the size of the γ' phase, the easier it is to be sheared by dislocations, and thus the earlier and more pronounced the softening appears. In addition, the coarsening of the precipitated γ' phase and its dissolution also reduce the pinning action of dislocations, and the

Fig. 15 Fracture morphology of HT700P alloy at different strain amplitude at 700 °C: (a), (c), (e) 0.3%; (b), (d), (f) 0.7%

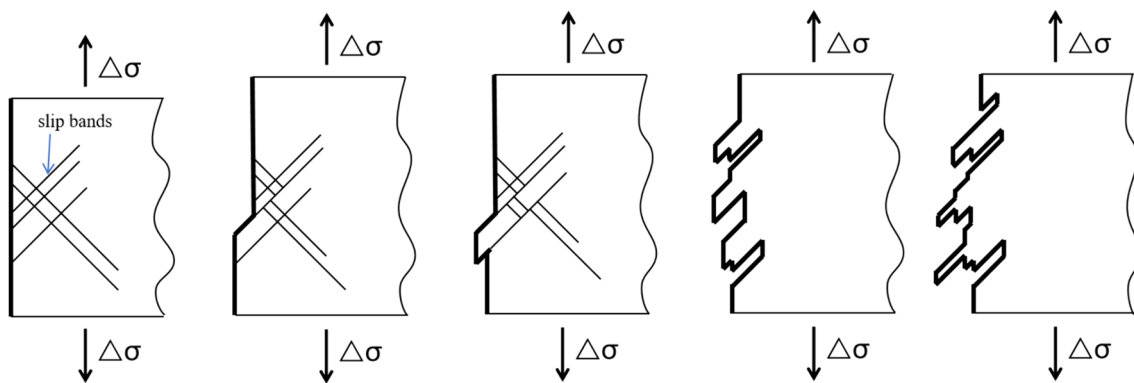
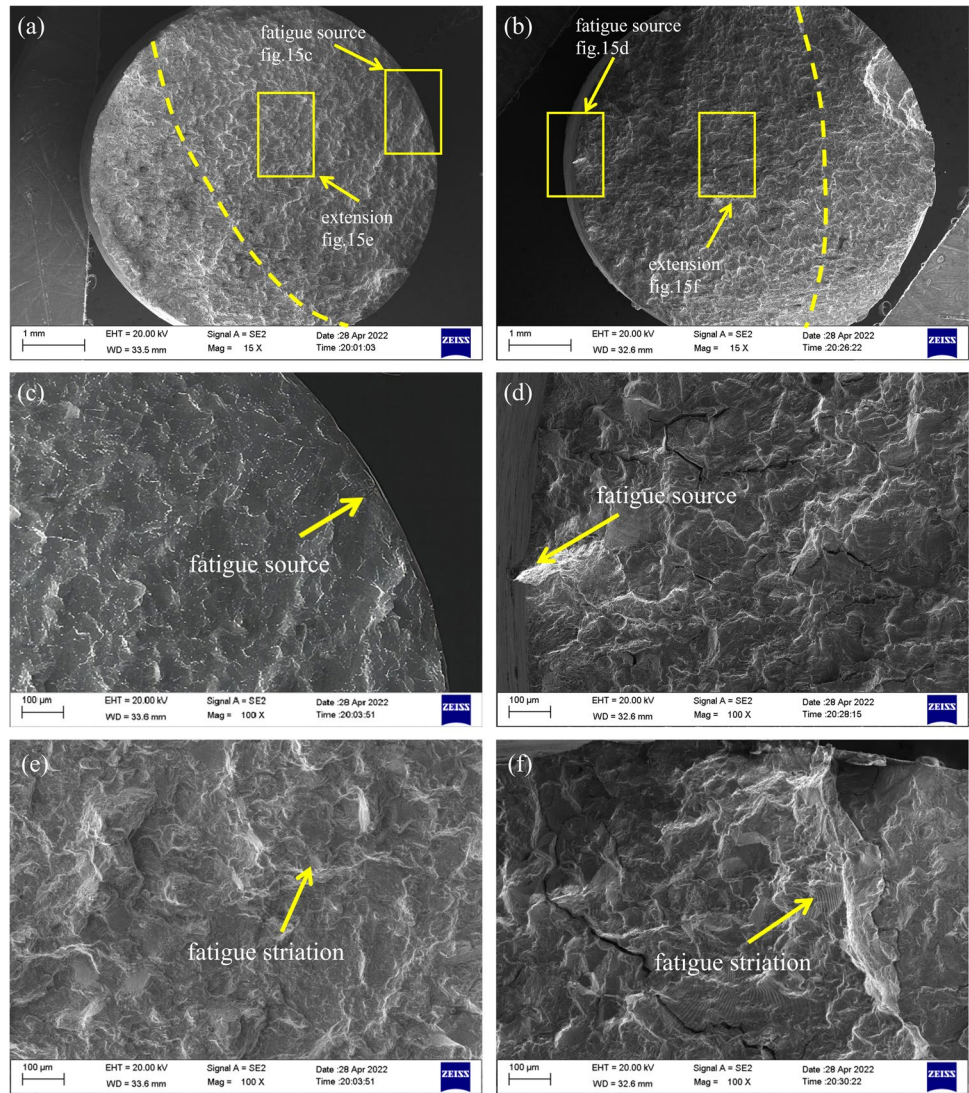


Fig. 16 Schematic diagram of microcracks caused by slip bands

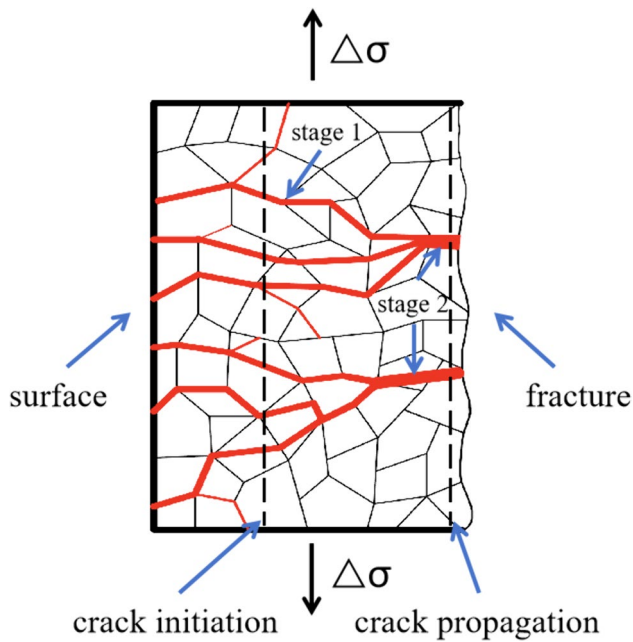


Fig. 17 Schematic diagram of microcrack initiation and propagation

slipping dislocations passing through the γ' phase precipitated phase by climbing or bypassing is the main reason for the occurrence of softening at the end of the cycle [33].

The samples with a strain amplitude of 0.3% showed cyclic hardening in the mid-fatigue stage, mainly due to the interaction between dislocations, between dislocations and precipitated phases, and the obstruction of dislocations by grain boundaries during the fatigue cyclic deformation process. This can strongly impede the movement of dislocations, causing them to become plugged, thus requiring an increased applied load to maintain a constant strain, leading to an increase in cyclic stress and the occurrence of cyclic strain hardening [24]. It should be noted, however, that cyclic hardening and cyclic softening of materials can only indicate the increase and decrease of strengthening with strain, and cannot affect the length of fatigue life [34].

Through comparison, it is found that the effect of γ' phase size on the low-cycle fatigue slip characteristics of HT700P high-temperature alloy is significant. The gap between structures with different γ' phase sizes in the spacing of slip bands is not obvious, but the tendency of multi-system slip in structures with smaller γ' phase sizes is larger than that in structures with larger γ' phase sizes, and the number of slip bands is greater. The γ' phase hinders the motion of slip bands, and since both grain boundaries and twin boundaries can hinder the motion of slip bands, it leads to the superposition of slip bands at grain boundaries and the formation of stress concentration at grain boundaries, which increases

energy consumption and thus slows down the expansion of slip bands [35].

5 Conclusion

Fatigue experiments were conducted on HT700P nickel–iron-based high-temperature alloy with different strain amplitudes at 650°C and 700°C. The main conclusions concerning the deformation behavior and fracture characteristics derived from this study are as follows:

1. The HT700P alloy exhibits overall cyclic softening characteristics in high-temperature low-week fatigue, which, combined with TEM analysis, indicates that this cyclic softening is related to the dislocation cut γ' phase as well as the coarsening of the γ' phase size.
2. The microscopic mechanism of HT700P high-temperature alloy low-cycle fatigue is mainly plane slip. Materials with relatively small γ' phase sizes have a greater tendency to exhibit multi-system slip.
3. Under the same strain amplitude, the larger the γ' phase size, the faster the crack extension rate, resulting in a shorter fatigue life of the alloy. Fatigue fracture morphology analysis shows that fatigue cracks initiate from the sample surface. However, in the sample tested at 700°C with a strain amplitude of 0.7%, the fatigue crack propagates along the crystal through mixed-mode expansion, while the rest of the samples also show fatigue cracks initiating from the surface but expanding along the crystal mixing expansion.

Acknowledgements This work was supported by State Key Laboratory for Mechanical Behavior of Materials (Grant No.20232508) and Excellent Youth Science and Technology Fund Project of Xi'an University of Science and Technology (Grant No. 6310221009).

Data availability The raw/processed data needed to generate these findings cannot be shared now, as they are also part of ongoing research.

Declarations

Competing interest The authors declare that they have no known competing financial interests or personal relationships that might affect the work reported herein.

References

1. G. Zhou, S. Bian, Z. Chen, Z. Chen, H. Bao, N. Zhang, Experimental study of high-temperature low cycle fatigue performance of inconel 617 and c-hra-2 alloys for advanced ultra-supercritical units. *J. Chin. Soc. Power Eng.* **42**, 475–83 (2022)

2. J. Bugge, S. Kjær, R. Blum, High-efficiency coal-fired power plants development and perspectives. *Energy* **31**(10–11), 1437–1445 (2006)
3. Y.X. Wang, W.Z. Feng, Efficient and clean coal-fired technology: 700°C ultra-supercritical coal-fired power generation technology, in 7th International Symposium on Advances in Electrical, Electronics, and Computer Engineering, vol. 12294 (SPIE, 2022), pp. 286–290
4. H. Nomoto, in *Advances in steam turbines for modern power plants* (Elsevier, 2017), pp. 263–278
5. D.S. Bhiogade, Ultra supercritical thermal power plant material advancements: a review. *J. Alloys Met. Syst.* **3**, 100024 (2023)
6. V. Viswanathan, R. Purgert, P. Rawls, Coal-fired power materials. *Adv. Mater. Process* **166**(8), 47–49 (2008)
7. M. Akbari-Garakani, M. Mehdizadeh, Effect of long-term service exposure on microstructure and mechanical properties of alloy 617. *Mater. Des.* **32**(5), 2695–2700 (2011)
8. N. Evans, P. Maziasz, R. Swindeman, G. Smith, Microstructure and phase stability in inconel alloy 740 during creep. *Scripta Mater.* **51**(6), 503–507 (2004)
9. M. Fukuda, in *Materials for ultra-supercritical and advanced ultra-supercritical power plants* (Elsevier, 2017), pp. 733–754
10. E.W. Huang, R.I. Barabash, Y. Wang, B. Clausen, L. Li, P.K. Liaw, G.E. Ice, Y. Ren, H. Choo, L.M. Pike et al., Plastic behavior of a nickel-based alloy under monotonic-tension and low-cycle-fatigue loading. *Int. J. Plast.* **24**(8), 1440–1456 (2008)
11. H. Pang, P. Reed, Effects of microstructure on room temperature fatigue crack initiation and short crack propagation in udimet 720li ni-base superalloy. *Int. J. Fatigue* **30**(10–11), 2009–2020 (2008)
12. B. Li, J. Yang, Z. Wang, G. Chen, X. Chen, Low cycle fatigue behavior of 316ln stainless steel: Effects of temperature, strain rate and strain amplitude. *Int. J. Fatigue* **175**, 107767 (2023)
13. L. Xiao, D.L. Chen, M.C. Chaturvedi, Shearing of γ "precipitates and formation of planar slip bands in Inconel 718 during cyclic deformation. *Scripta Mater.* **52**(7), 603–607 (2005)
14. M. Clavel, A. Pineau, Fatigue behaviour of two nickel-base alloys I: Experimental results on low cycle fatigue, fatigue crack propagation and substructures. *Mater. Sci. Eng.* **55**(2), 157–171 (1982)
15. D. Fournier, A. Pineau, Low cycle fatigue behavior of Inconel 718 at 298 K and 823 K. *Metall. Trans. A* **8**, 1095–1105 (1977)
16. G. Chen, Y. Zhang, D. Xu, Y. Lin, X. Chen, Low cycle fatigue and creep-fatigue interaction behavior of nickel-base superalloy gh4169 at elevated temperature of 650 c. *Mater. Sci. Eng., A* **655**, 175–182 (2016)
17. J. Xie, D. I. Shu, G.C. Hou, J.J. Yu, Y.Z. Zhou, X.F. Sun, Low-cycle fatigue behavior of k416b ni-based superalloy at 650° c. *J. Centr. South Univ* **28**(9), 2628–2635 (2021)
18. A. Cervellon, S. H'emery, P. K'urnsteiner, B. Gault, P. Kontis, J. Cormier, Crack initiation mechanisms during very high cycle fatigue of ni-based single crystal superalloys at high temperature. *Acta Materialia* **188**, 131–144 (2020)
19. R. Viswanathan, J. Henry, J. Tanzosh, G. Stanko, J. Shingledecker, B. Vitalis, R. Purgert, Us program on materials technology for ultra-supercritical coal power plants. *J. Mater. Eng. Perform.* **14**, 281–292 (2005)
20. S. Wee, K. Kim, K. Park, C. Seok, Study on creep damage of ni-based superalloy caused by variable load conditions at elevated temperatures. *Materials* **14**(22), 6971 (2021)
21. Q. Wang, Y. Wu, J. Chen, J. Song, C. Xiao, X. Hui, Enhancement of high temperature low cycle fatigue lifetime of pwa1484 superalloy artificial bicrystals via boron-induced grain boundary strengthening. *Int. J. Fatigue* **165**, 107223 (2022)
22. I.M. Lifshitz, V.V. Slyozov, The kinetics of precipitation from supersaturated solid solutions. *J. Phys. Chem. Solids* **19**(1–2), 35–50 (1961)
23. C. Wagner, Theorie der alterung von niederschlagungen durch uml'osen (ostwaldreifung). *Zeitschrift f'ur Elektrochemie, Berichte der Bunsengesellschaft f'ur physikalische Chemie* **65**(7–8), 581–591 (1961)
24. S. Suresh, *Fatigue of materials* (Cambridge University Press, 1998)
25. D. Hull, D.J. Bacon, *Introduction to dislocations* (Butterworth-Heinemann, 2001)
26. C. Laird, in *Fatigue crack propagation* (ASTM International, 1967)
27. K. Tanaka, T. Mura, A dislocation model for fatigue crack initiation. *J. Appl. Mech.* **48**(1), 97–103 (1981)
28. T.L. Anderson, T.L. Anderson, *Fracture mechanics: fundamentals and applications* (CRC Press, 2005)
29. D. Kim, R. Jiang, A. Evangelou, I. Sinclair, P. Reed, Effects of γ size and carbide distribution on fatigue crack growth mechanisms at 650° c in an advanced ni-based superalloy. *Int. J. Fatigue* **145**, 106086 (2021)
30. L. Wang, S. Wang, X. Song, Y. Liu, G. Xu, Effects of precipitated phases on the crack propagation behaviour of a ni-based superalloy. *Int. J. Fatigue* **62**, 210–216 (2014)
31. W. Walston, K. O'hara, E. Ross, T. Pollock, W. Murphy, Renfin6: third generation single crystal superalloy. *Superalloy* 27–34 (1996)
32. J. Sato, T. Omori, K. Oikawa, I. Ohnuma, R. Kainuma, K. Ishida, Cobalt-base high-temperature alloys. *Science* **312**(5770), 90–91 (2006)
33. T. Jin, Y. Zhou, X. Wang, J. Liu, X. Sun, Z. Hu, Research process on microstructural stability and mechanical behavior of advanced ni-based single crystal superalloys. *Acta Metall Sin* **51**(10), 1153–1162 (2015)
34. G. Yuanyuan, Z. Yunsong, Z. Jiang, L. Yanfei, L. Yushi, S. Jiangbo, Effect of strain amplitude on cyclic deformation behavior of nickel-based single crystal superalloy dd11 in low cycle fatigue. *Rare Metal Mater. Eng* **48**(2), 366–374 (2019)
35. H. Deng, L. Wang, Y. Liu, X. Song, F. Meng, T. Yu, Fatigue crack propagation behavior of IN718 superalloy aged with temperature/stress coupled field. *Int. J. Fatigue* **153**, 106514 (2021)

Springer Nature or its licensor (e.g. a society or other partner) holds exclusive rights to this article under a publishing agreement with the author(s) or other rightsholder(s); author self-archiving of the accepted manuscript version of this article is solely governed by the terms of such publishing agreement and applicable law.